

# Oxford SWIFT IFS and multi-wavelength observations of the Eagle galaxy at $z=0.77$

Susan A. Kassin,<sup>1,2\*</sup> L. Fogarty,<sup>1</sup> T. Goodsall,<sup>1,3</sup> F. J. Clarke,<sup>1</sup> R. W. C. Houghton,<sup>1</sup> G. Salter,<sup>1</sup> N. Thatte,<sup>1</sup> M. Tecza,<sup>1</sup> Roger L. Davies,<sup>1</sup> Benjamin J. Weiner,<sup>4</sup> C. N. A. Willmer,<sup>4</sup> Samir Salim,<sup>5</sup> Michael C. Cooper,<sup>6</sup> Jeffrey A. Newman,<sup>7</sup> Kevin Bundy,<sup>8</sup> C. J. Conselice,<sup>9</sup> A. M. Koekemoer,<sup>10</sup> Lihwai Lin,<sup>11</sup> Leonidas A. Moustakas,<sup>3</sup> Tao Wang<sup>12</sup>

<sup>1</sup> Sub-Department of Astrophysics, University of Oxford, Denys Wilkinson Building, Keble Road, Oxford OX1 3RH, UK

<sup>2</sup> currently: Astrophysics Science Division, Goddard Space Flight Center, Code 665, Greenbelt, MD 20771, USA

<sup>3</sup> Jet Propulsion Laboratory, California Institute of Technology, 4800 Oak Grove Drive, MS 169-327, Pasadena, CA 91109, USA

<sup>4</sup> Steward Observatory, 933 N. Cherry St., University of Arizona, Tucson, AZ 85721, USA

<sup>5</sup> Department of Astronomy, Indiana University, Bloomington, IN 47404, USA

<sup>6</sup> Center for Galaxy Evolution, Department of Physics and Astronomy, University of California, Irvine,

4129 Frederick Reines Hall, Irvine, CA 92697, USA; Hubble Fellow

<sup>7</sup> Department of Physics and Astronomy, University of Pittsburgh, 3941 O'Hara Street, Pittsburgh, PA 1526, USA

<sup>8</sup> Astronomy Department, University of California, Berkeley, CA 94705, USA; Hubble Fellow

<sup>9</sup> University of Nottingham, School of Physics and Astronomy, Nottingham NG7 2RD, UK

<sup>10</sup> Space Telescope Science Institute, 3700 San Martin Drive, Baltimore, MD 21218, USA

<sup>11</sup> Institute of Astronomy & Astrophysics, Academia Sinica, Taipei 106, Taiwan

<sup>12</sup> Harvard-Smithsonian Center for Astrophysics, 60 Garden Street, Cambridge, MA 02138, USA

1 March 2022

## ABSTRACT

The ‘Eagle’ galaxy at a redshift of 0.77 is studied with the Oxford Short Wavelength Integral Field Spectrograph (SWIFT) and multi-wavelength data from the All-wavelength Extended Groth strip International Survey (AEGIS). It was chosen from AEGIS because of the bright and extended emission in its slit spectrum. Three dimensional kinematic maps of the Eagle reveal a gradient in velocity dispersion which spans  $35 - 75 \pm 10 \text{ km s}^{-1}$  and a rotation velocity of  $25 \pm 5 \text{ km s}^{-1}$  uncorrected for inclination. *Hubble Space Telescope* images suggest it is close to face-on. In comparison with galaxies from AEGIS at similar redshifts, the Eagle is extremely bright and blue in the rest-frame optical, highly star-forming, dominated by unobscured star-formation, and has a low metallicity for its size. This is consistent with its selection. The Eagle is likely undergoing a major merger and is caught in the early stage of a star-burst when it has not yet experienced metal enrichment or formed the mass of dust typically found in star-forming galaxies.

**Key words:** galaxies: high-redshift, galaxies – galaxies: kinematics and dynamics – galaxies: interactions – galaxies: irregular.

## 1 INTRODUCTION

Large redshift surveys at  $0 < z < 1.2$  have revealed that the population of galaxies is divided into red and blue rest-frame colours, and have measured the evolution of these populations (e.g., Strateva et al. 2001; Bell et al. 2004; Faber et al. 2007). In particular, blue galaxies in

the past were brighter by  $B \simeq 1.3 \text{ mag}$  (e.g., Bell et al. 2004; Willmer et al. 2006), more highly star-forming (e.g., Noeske et al. 2007), and more morphologically irregular (e.g., Abraham et al. 1996; Oesch et al. 2010). In addition, blue galaxies have an increasing contribution to their kinematics from disordered motions the further one looks back in time (Weiner et al. 2006a; Kassin et al. 2007).

These disordered motions, quantified by an inte-

\* E-mail: susan.kassin@nasa.gov

grated velocity dispersion, appear to play an important role in galaxy kinematics (e.g., Weiner et al. 2006b; Kassin et al. 2007; Cresci et al. 2009; Covington et al. 2010; Förster Schreiber et al. 2009; Puech et al. 2010; Lemoine-Busserolle et al. 2010; Lemoine-Busserolle & Lamareille 2010). A study of  $\sim 550$  galaxies with slit spectroscopy over  $0.1 < z < 1.2$  has shown that, for galaxies with stellar masses greater than  $10^{10} M_{\odot}$ , there is increasing scatter in the Tully-Fisher relation (which relates the rotation velocities of galaxies to their stellar masses or magnitudes) to  $z = 1.2$  (Kassin et al. 2007). This scatter is dominated by galaxies with disturbed morphologies (Kassin et al. 2007). A large scatter in the Tully-Fisher relation is also found for galaxies in integral field spectrograph (IFS) studies at  $z \sim 0.6$  (Flores et al. 2006; Puech et al. 2008, 2010) and  $z \sim 2 - 3$  (e.g., Law et al. 2009; Cresci et al. 2009; Lemoine-Busserolle & Lamareille 2010).

When a kinematic estimator which incorporates both rotation velocity ( $V$ ) and integrated velocity dispersion ( $\sigma$ ) is adopted,  $S_K \equiv \sqrt{KV^2 + \sigma^2}$  with  $K=0.5$  (Weiner et al. 2006a), the resulting relation with stellar mass has remarkably small scatter at all redshifts (Kassin et al. 2007; Cresci et al. 2009; Covington et al. 2010; Puech et al. 2010; Lemoine-Busserolle et al. 2010; Lemoine-Busserolle & Lamareille 2010). This is such that disturbed galaxies have higher values of  $\sigma$  than normal disc-like galaxies. Undisturbed disc galaxies in the local Universe have  $\sigma$  values that range from  $10\text{--}35 \text{ km s}^{-1}$  and an average value of  $\sim 20\text{--}25 \text{ km s}^{-1}$  (Epinat et al. 2010) which are due to the relative motions of individual gas clouds in spiral arms or a thick disc. The higher  $\sigma$  values found for many high redshift galaxies likely represent effective velocity dispersions caused by the blurring of velocity gradients on scales at or below the seeing limit (Weiner et al. 2006a; Kassin et al. 2007). These may not even have a preferred plane.

The nature of these kinematically peculiar objects cannot be fully determined from slit spectroscopy alone since it is unable to probe the full 3D kinematics of galaxies. 3D integral field observations can give further clues as to whether the high  $\sigma$  values are driven by phenomena such as rotation, major or minor merger activity, and/or violent star-formation processes.

The advent of IFSs on large telescopes has allowed for detailed studies of 3D galaxy kinematics over  $0.4 \lesssim z \lesssim 3$  (e.g., Förster Schreiber et al. 2006, 2009; Puech et al. 2007; Yang et al. 2008; van Starkenburg et al. 2008; Wright et al. 2009; Law et al. 2009; Epinat et al. 2009; Lemoine-Busserolle et al. 2010; Lemoine-Busserolle & Lamareille 2010). These studies have all found galaxies with large  $\sigma$  values and attribute it to star-formation and major and minor merger activity, when active galactic nuclei are not present. However, these samples are still small ( $\lesssim 100$ ) and are typically too bright to be representative of typical galaxies, although there are exceptions (e.g., Puech et al. 2008; Yang et al. 2008; Law et al. 2009).

A representative sample of 68 galaxies at redshifts  $0.4 < z < 0.74$  has been studied with the GIRAFFE IFS with the Intermediate MAss Galaxy Evolution Sequence (IMAGES) Survey. Two main results of this survey are the discovery of a low fraction of rotating disc galaxies

(Flores et al. 2006; Neichel et al. 2008; Yang et al. 2008) and the finding that more distant galaxies have smaller ratios of  $V$  to  $\sigma$  than galaxies at lower redshifts (Puech et al. 2007). These results are consistent with the findings of slit based studies of larger samples of  $\sim 500\text{--}1000$  galaxies (Weiner et al. 2006a,b; Kassin et al. 2007). Studies of IM-AGES galaxies generally attribute disturbed kinematics to major mergers.

It is highly desirable to study more galaxies with IFSs at  $z \sim 1$ , an epoch probed by large redshift surveys but with few IFS observations. In this paper, IFS observations of the 3D kinematics of a galaxy at  $z = 0.7686$  with a high  $\sigma$  value are presented along with a suite of multi-wavelength data from the All-wavelength Extended Groth strip International Survey (AEGIS, Davis et al. 2007). These data allow for the galaxy to be understood in terms of the general population of galaxies at its epoch and offer insight into a likely cause for its high  $\sigma$  value. A  $\Lambda$ CDM cosmology is adopted throughout:  $H = 70 \text{ km s}^{-1} \text{ Mpc}^{-1}$ ,  $\Omega_m = 0.3$ ,  $\Omega_{\Lambda} = 0.7$ . All logarithms are base 10, and all magnitudes are on the AB system.

## 2 THE EAGLE GALAXY

### 2.1 Selection

The Eagle galaxy, DEEP2 ID 13019195 ( $\alpha 14:19:39.3$ ,  $\delta +52:55:48.8$ , J2000), was selected from the AEGIS Survey (for which the DEEP2 Survey provides redshifts and spectra; Davis et al. 2003) to be observed with the Oxford Short Wavelength Integral Field Spectrograph (SWIFT; Thatte et al. 2006). The Eagle galaxy is so named for its distinctive appearance in *Hubble Space Telescope* images (Figures 1 and 2). It was primarily selected from the AEGIS Survey to have very bright and extended line emission ( $\gtrsim 10^{-16} \text{ ergs s}^{-1} \text{ cm}^{-2}$  and  $\gtrsim 2''$  from a visual inspection of the spectrum, respectively) which falls into the SWIFT bandpass. The aim of these requirements was to provide a target which would result in observations with a high signal-to-noise ratio and at least two independent spatial resolution elements. The [OIII]  $\lambda 5007$  emission line in the DEEP2 spectrum of the Eagle has an integrated flux of  $9.6(\pm 2.5) \times 10^{-16} \text{ ergs s}^{-1} \text{ cm}^{-2}$  and a spatial extent of  $\gtrsim 2''$  from a visual inspection.

The target was further required to have at least one emission line not contaminated by sky lines, a redshift greater than  $\simeq 0.7$ , an inclination  $\lesssim 70^\circ$ , and a significant  $\sigma$  ( $> 40 \text{ km s}^{-1}$ ). The limit on inclination allows for kinematics to be studied across the face of the galaxy without significant projection effects, and the requirement on  $\sigma$  allows for an investigation into the cause of the unusually high  $\sigma$  values found for galaxies at high redshift.

### 2.2 Hubble morphology & size

#### 2.2.1 Morphology

*Hubble*/ACS *V*-band and *V* + *I*-band images are shown in Figures 1 and 2, respectively. Quantitative morphological analyses were performed on the *I*-band image with the CAS and Gini/M<sub>20</sub> systems (Conselice et al. 2003 and Lotz, Primack, & Madau 2004, respectively). Both

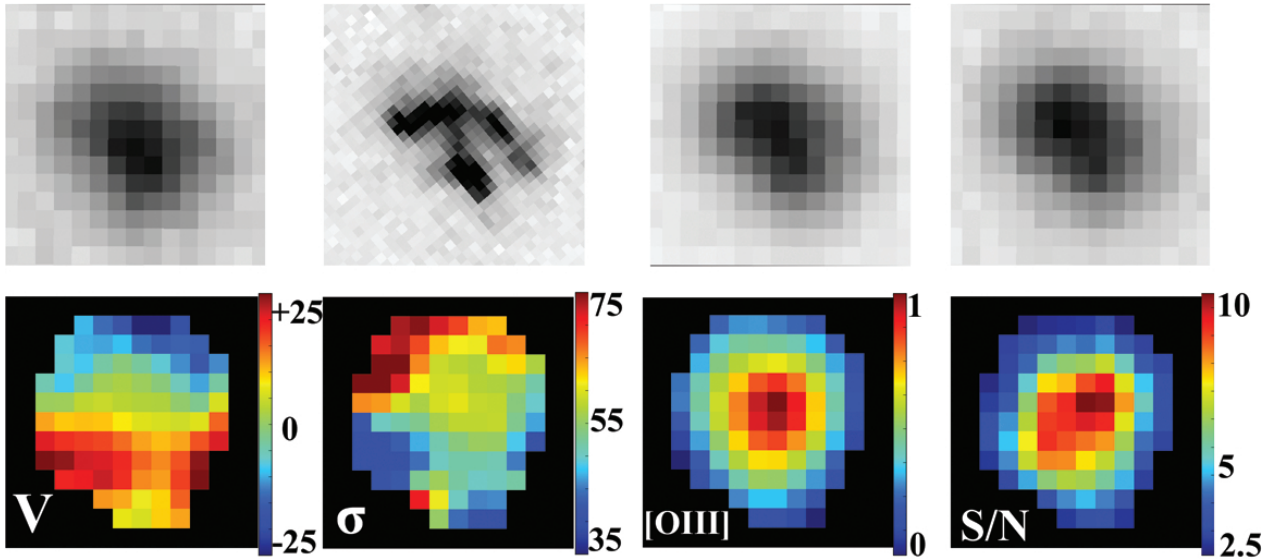


**Figure 1.** Broad-band and SWIFT IFS observations of the Eagle galaxy are shown in the top and bottom panels, respectively. All panels are  $3''$  on a side and are oriented such that north is up and east is to the left. Top row: Broad-band images at  $B$  (CFHT/CFH12K;  $0.21''\text{pixel}^{-1}$ ),  $V$  (*Hubble*/ACS;  $0.1''\text{pixel}^{-1}$ ),  $R$  (CFHT), and  $I$  (CFHT) are shown from left to right. The image FWHM for the CFHT images was  $\sim 0.7''$ . Bottom row: Maps of  $V$ ,  $\sigma$ , [OIII] line emission, and signal-to-noise ratio for the [OIII] line are shown from left to right. These maps have been smoothed with a Gaussian with a  $\sigma$  of 1 spaxel ( $0.235''$ ), which is much smaller than the  $\sim 1''$  image FWHM during the observations. Due to similar image FWHMs, the most direct comparison can be made between the SWIFT observations and the broad-band images from CFHT.

classify the Eagle as a major merger galaxy. Specifically, the Eagle has an asymmetry ( $A$ ) value of 0.32 (Lin et al. 2007), and although major mergers are defined in CAS as galaxies with  $A \geq 0.35$ , once the signal-to-noise in the ACS image is taken into account, it is classified as such. In addition, Lin et al. (2007) classify galaxies with  $A > 0.25$  as major mergers. The Eagle has Gini and  $M_{20}$  values of 0.46 and -0.91, respectively (Lotz et al. 2008). These qualify it as a major merger according to the definition in Lotz et al. (2008):  $\text{Gini} > -0.14M_{20} + 0.33$ .

Furthermore, according to the visual classification of *Hubble* images in Kassin et al. (2007) which categorised galaxies as ‘normal’, ‘disturbed’, or ‘compact’, the Eagle is identified as ‘disturbed.’ This is mainly due to outer isophotes which are not elliptical and an asymmetric three-armed structure, both of which are inconsistent with the morphology of an undisturbed disc galaxy. In summary, quantitative and qualitative morphological classifications of the Eagle are consistent with it being a major merger galaxy and inconsistent with it being a disc galaxy.

### 2.2.2 Size

It is difficult to measure the sizes of high redshift galaxies which are not always smooth or elliptical. In order to avoid biases due to disturbed morphologies, we look to measure a constant fraction of the total galaxy light, independent of the morphology or orientation of the object. The Petrosian radius comes closest to this ideal (e.g., Petrosian 1976; Bershady et al. 2000; Massey et al. 2004). Petrosian radii measured in elliptical apertures are adopted from Lotz et al. (2008). The radii were measured from  $I$ -band *Hubble* images using the SExtractor

software (Bertin & Arnouts 1996) for  $\eta = 0.2$ . The Petrosian radius of the Eagle is  $1.2'' \pm 0.2''$ , which corresponds to 8.9 kpc at its redshift, and the position angle of the major axis is  $49^\circ$  (east of north).

## 3 SWIFT OBSERVATIONS AND DATA REDUCTION

The Eagle Galaxy was observed under clear conditions with SWIFT mounted on the Hale Telescope at Palomar Observatory on May 8th, 9th, and 10th of 2009. Observations were performed in natural seeing mode in the coarsest spaxel scale of  $0.235''$ , which results in a field of view of  $10.3'' \times 20.9''$ . The spectral resolution at the observed wavelength of  $8855\text{\AA}$  is  $R \sim 4000$ , which results in an instrumental broadening of  $\simeq 1.2\text{\AA}$  or  $41\text{ km s}^{-1}$  (Gaussian  $\sigma = 21\text{ km s}^{-1}$ ), as measured from fits of line profiles to isolated sky lines near the observed wavelength. To obtain an accurate pointing, the telescope was offset blindly from a nearby bright star to the galaxy. The large field of view allowed for dithering on source, and integrations of 900s each were taken. During this commissioning run we were unable to guide the telescope, and relied on tracking alone. A total of 6 exposures which had the best delivered image quality, or image FWHM, were chosen to create the final cube, resulting in a total exposure time of 1.5 hours. The image FWHM was  $\sim 1''$  for these observations; they were taken at the beginnings of the nights of May 9th and 10th.

The SWIFT data were reduced with custom-purpose software written by R. Houghton and T. Goodsall, based on the *spread* pipeline for the SINFONI IFS (Schreiber et al. 2004; Abuter et al. 2006). The SWIFT reduction pro-

cedure is described in detail in Fogarty et al. (2010), and is briefly reviewed here. The galaxy was observed in one of the two CCDs, so only data from that CCD was processed. All frames were reduced in the same manner. First the bias was removed, the overscan region trimmed, and cosmic rays removed with the L.A.Cosmic algorithm (van Dokkum 2001). A wavelength solution was found from Ar and Ne arc lamp exposures taken at the beginning of the observing run. Any flexure in wavelength between observations was quantified by measuring the shift of sky lines close to the [OIII] line in wavelength. For 2 of the 6 exposures used, there was flexure in the wavelength axis of 0.46 and 0.49 of a pixel (1 pixel = 1 Å). These cubes were shifted in wavelength to align them with the other observations using a third order spline interpolation.

Since dithering was performed on source, sky subtraction could be accomplished with the subtraction of AB pairs of observations. To obtain optimal sky subtraction, “super skys” were created by taking the median of the 2 or 3 A or B observations closest in time to each B and A observation, respectively. The sky subtracted data cubes were aligned spatially on the peak flux of the [OIII] line map of the galaxy and co-added.

### 3.1 Kinematic maps

To measure kinematics from the final co-added data cube, Gaussian functions were fit to the [OIII] line in the spectrum of each spatial pixel in which the galaxy was detected. The resulting rotation velocity ( $V$ ), velocity dispersion corrected for instrumental broadening ( $\sigma$ ), [OIII] line, and signal-to-noise maps are shown in Figure 1. The maps have been smoothed spatially with a Gaussian  $\sigma$  of 1 pixel (1 spaxel = 0.235"), which is much less than the image FWHM of  $\sim 1''$ , to decrease pixel-to-pixel noise. A signal-to-noise threshold of 2.5 was applied to these maps.

Also shown in Figure 1 are ground-based images from the Canada-France-Hawaii Telescope (CFHT)/CFH12k camera at  $B$ ,  $R$ , and  $I$ , and a  $V$ -band image from *Hubble*/Advanced Camera for Surveys (ACS). The most direct comparison for the SWIFT observations is to the CFHT images, rather than the *Hubble* image, since the image FWHM for the CFHT images is  $\sim 0.7''$ , similar to that during the SWIFT observations ( $\sim 1''$ ). Figure 1 shows that the morphology of the Eagle galaxy does not vary significantly from observed  $B$  to  $I$  in the CFHT images. The SWIFT O[III] linemap has a similar morphology to the CFHT broad-band images, but is less irregular-shaped, consistent with a poorer image FWHM. The number of spatial elements per resolution element (i.e., the oversampling rate) for the SWIFT maps is  $\sim 4$ .

The  $V$  map is consistent with a maximum value of  $V \times \sin(i)$  of  $25 \pm 5 \text{ km s}^{-1}$ , where  $i$  is the inclination of the galaxy. This is the maximum rotation spread along a line with a position angle of  $145^\circ$  (measured east of north). From a visual inspection of the *Hubble* images, it is clear that the Eagle has isophotes which are not ellipsoidal and an asymmetric three-armed structure. In addition, the kinematic major axis is not aligned with

the morphological major axis. (The direction of the morphological major axis is the same as the position angle of the slit for the DEEP2 observations; see §4.5 and Figure 2.) Both of these findings are inconsistent with the Eagle being an edge-on disc. It is more likely that this galaxy is viewed nearly face-on, i.e. with an inclination  $\lesssim 30^\circ$ . We refrain from measuring the inclination due to the large uncertainties inherent in measuring low inclinations, especially for systems with isophotes which are not ellipsoidal. For inclinations of  $30^\circ$ ,  $20^\circ$ ,  $10^\circ$ , and  $5^\circ$ , the inclination-corrected  $V$  varies systematically from 50–287  $\text{km s}^{-1}$ , namely  $V = 50, 73, 144$ , and  $287 \text{ km s}^{-1}$ , respectively.

The  $\sigma$  field shows a gradient such that the southern and northern sections of the galaxy have typical  $\sigma$ 's of  $35 - 50$  and  $65 - 75 \text{ km s}^{-1}$ , respectively, with uncertainties of  $10 \text{ km s}^{-1}$ . As mentioned in §1, undisturbed disc galaxies in the local Universe have  $\sigma$  values that range from  $10 - 35 \text{ km s}^{-1}$  and an average value of  $\sim 20 - 25 \text{ km s}^{-1}$  (Epinat et al. 2010) which are due to the relative motions of individual gas clouds in spiral arms or a thick disc. The much higher  $\sigma$  values found for the Eagle likely represent effective velocity dispersions caused by the blurring of velocity gradients on scales at or below the seeing limit (Weiner et al. 2006a; Kassin et al. 2007). These may not even have a preferred plane. In addition, the northern edge of the Eagle, where the highest  $\sigma$  values occur, is where the three “arms” of the galaxy which are visible in the *Hubble* images meet, possibly indicative of tidal disturbances there.

For a rotating disc galaxy observed at high redshift, seeing (i.e., beam smearing) smooths out the  $V$  gradient and produces a strong peak in the centre of the  $\sigma$  map (e.g., Weiner et al. 2006a; Covington et al. 2010). The  $\sigma$  peak is produced in the central parts of the galaxy where the velocity gradient is strongest and seeing smears the light from gas at different velocities together. There is no seeing-induced peak observed in the  $\sigma$  field of the Eagle. This is likely due to a combination of its low value of  $V \times \sin(i)$  and correspondingly shallow velocity gradient in its inner parts, and low spatial resolution. For an image FWHM of  $\sim 1''$ , the resulting decrement in  $V$ , which is typically  $\sim 10 - 15 \text{ km s}^{-1}$  for a galaxy the size of the Eagle (Weiner et al. 2006a; Kassin et al. 2007), is significantly less than the range in  $V$  allowed due to the uncertainty in the inclination ( $\pm \sim 95 \text{ km s}^{-1}$ ). Due to this, the low spatial resolution of the 3D maps, and the misalignment of the kinematic and morphological major axes, we refrain from creating a detailed kinematic model for this system.

### 3.2 Comparison with kinematics of galaxies at the same epoch

In Figure 3, the kinematics of the Eagle are compared with those of a sample of galaxies at the same epoch in terms of the ratio of  $V$  to  $\sigma$ , as measured in Kassin et al. (2007). These galaxies are essentially selected on emission line strength and are  $\gtrsim 80\%$  complete down to  $\sim 10^{9.5} M_\odot$  (Kassin et al. 2007). For the Eagle, the range of allowed values of  $V$  from §3.1, and an average  $\sigma$  over the

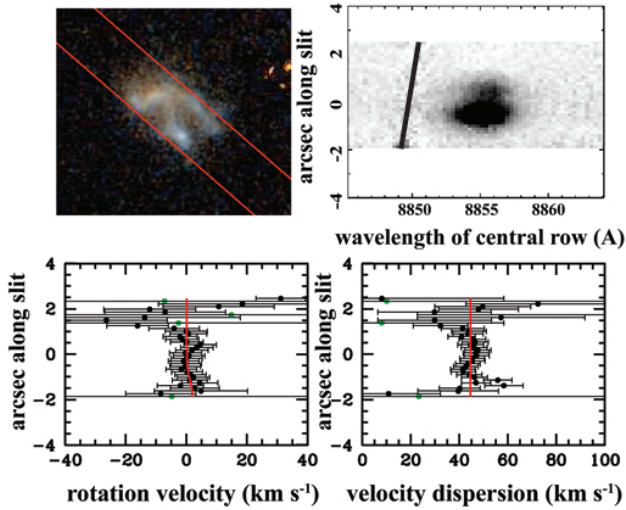


**Figure 2.** *Hubble* and DEIMOS observations of the Eagle galaxy (top) and fits to the kinematics (bottom). In the upper left panel is a colour *Hubble* image created from  $V$  and  $I$ -band exposures with the position of the  $1''$  wide DEIMOS slit marked. It is oriented such that north is up and east is to the left. The upper right panel shows the [OIII] line in the slit spectrum. The spectrum is shown as observed, so constant wavelength runs diagonally (black line). The lower panels show the rotation and dispersion profiles created by Gaussian fits to each row of pixels in the [OIII] line. The black points are data used, and the green points are rejected. Note that not all points are independent due to the  $\sim 0.7''$  seeing. The solid red lines are the best fit kinematic models described in §4.1.

entire galaxy of  $55 \pm 10 \text{ km s}^{-1}$ , are adopted. Galaxies in Figure 3 are coded according to the visual morphological classification from Kassin et al. (2007). It is apparent that galaxies with low  $V/\sigma$  values are generally classified as disturbed, whereas those with high values have normal disc-like morphologies. Galaxies in the IMAGES Survey at  $z \sim 0.6$  show a similar range in  $V/\sigma$  (Puech et al. 2007). Although the Eagle has a large allowable range in  $V/\sigma$  due to the large uncertainty in its inclination, it cannot be among the very  $V$ -dominated systems because of its large  $\sigma$  which, at its lowest possible value of  $45 \text{ km s}^{-1}$ , is still greater than that found for local galaxies (§1). This is consistent with the Eagle’s morphological classification as disturbed or major merger (§2.2).

#### 4 MULTI-WAVELENGTH DATA AND SPECTRAL ENERGY DISTRIBUTION FROM AEGIS

A few IFS studies have incorporated multi-wavelength data which span from the UV or optical to the far-infrared (e.g., Fuentes-Carrera et al. 2010; Hammer et al. 2009; Puech et al. 2009, 2010). Such data facilitate the formulation of more complete pictures of the galaxies by allowing for more accurate determinations of e.g., star-formation rates, dust content, and sometimes metallicity.

Multi-wavelength photometry and a flux calibrated optical spectrum come from the AEGIS Survey. The spec-

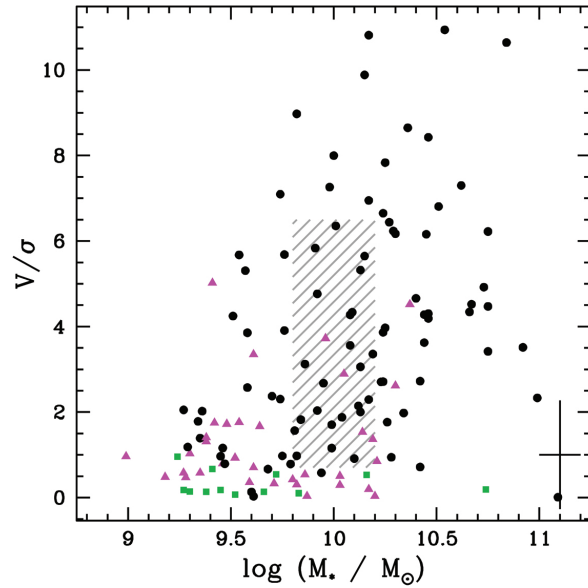


**Figure 3.** The range of values allowed for the ratio of rotation velocity to integrated velocity dispersion of the Eagle (grey shading) is compared to values for emission line galaxies at  $0.65 < z < 0.85$  from Kassin et al. (2007) as a function of stellar mass. The range in  $V/\sigma$  for the Eagle is mainly due to the uncertainty in its inclination. Other galaxies are coded according to their visual morphology as deduced from *Hubble* images by Kassin et al. (2007): normal (black points), disturbed (magenta triangles), and compact (green squares). A typical error bar for these galaxies is shown in black. Although the Eagle has a large uncertainty in  $V/\sigma$ , it is not among the very  $V$ -dominated systems at this epoch due to its large average  $\sigma$  which, at its lowest possible value of  $45 \text{ km s}^{-1}$ , is still greater than that found for local galaxies.

trum and redshift are from the DEEP2 Survey, a portion of which is incorporated into AEGIS. A far-infrared flux (observed  $24\mu\text{m}$ ) is adopted from the FIDEL Survey (Dickinson et al. in preparation) which overlaps AEGIS and has a greater depth than the AEGIS  $24\mu\text{m}$  imaging. Data are taken from the following telescope/instrument combinations: Keck-2/DEep Imaging Multi-Object Spectrograph (DEIMOS) for an optical spectrum, *Galaxy Evolution Explorer* for ultraviolet photometry, *Hubble Space Telescope*/Advanced Camera for Surveys (ACS) for optical imaging, Canada-France-Hawaii Telescope (CFHT)/CFH12K for optical imaging and photometry, Palomar/Wide Field Infrared Camera (WIRC) for  $K_s$ -band photometry, *Spitzer*/Infrared Array Camera (IRAC) for mid-infrared photometry, *Spitzer*/Multiband Imaging Photometry for *Spitzer* (MIPS) for  $24\mu\text{m}$  photometry, and Chandra/AXAF CCD Imaging Spectrometer (ACIS) for counts in the hard and soft bands. Data reduction is discussed in Davis et al. (2007) for AEGIS and Salim et al. (2009) for FIDEL.

Photometry was performed on these images as follows, and all measure total galaxy flux. For the CFHT images,  $R$ -band magnitudes were measured in circular apertures of radius  $3r_g$ , where  $r_g$  is the  $\sigma$  of a Gaussian fit to the image profile. To derive  $B$  and  $I$ -band magnitudes,

**Table 1.** Properties of the Eagle galaxy.

$V \sin(i)$ km s <sup>-1</sup>	$\sigma$ km s <sup>-1</sup>	SFR (total) M <sub>⊙</sub> yr <sup>-1</sup>	$M_*$ log M <sub>⊙</sub>	$M_B$ AB	$U - B$ AB	$12 + \log(O/H)$	$R_{I,Petrosian}$ "
$25 \pm 5$	$35 - 75 \pm 10$	$26.3 \pm 0.4$	$10.0 \pm 0.2$	$-21.51 \pm 0.08$	$0.46 \pm 0.09$	$8.66 \pm 0.05$	$1.2 \pm 0.2$

$B - R$  and  $R - I$  colours were measured in a  $1''$  radius aperture (Coil et al. 2004). The resulting  $B$  and  $I$ -band magnitudes differ from magnitudes measured within  $3r_g$  only if there are significant colour gradients in the CFHT images, which there are not (Figure 1). For the WIRC images, photometry was performed using a Kron-like aperture (Bundy et al. 2006). For the IRAC images, photometry was performed in a  $3''$  diameter aperture (Davis et al. 2007). For MIPS and GALEX images, since the point spread functions (PSFs) are  $6''$  and  $5''$  respectively, PSF fluxes were extracted.

K-corrections are applied following Willmer et al. (2006) to obtain rest-frame  $U$  and  $B$ -band magnitudes, which are given in Table 1. A rest-frame colour-magnitude diagram in Figure 4 shows all galaxies in AEGIS at  $0.65 < z < 0.85$ . It shows that the Eagle galaxy is extremely bright and blue compared to its contemporary galaxies.

#### 4.1 Single slit kinematics

We look to kinematics derived from the DEEP2 slit spectrum for complementarity and completeness. The [OIII] emission line in this spectrum is shown in Figure 2. The image FWHM is  $\sim 0.7''$ . The resolution was  $R \sim 5000$  and the slit width was  $1''$ , which resulted in a spectral resolution of FWHM =  $0.56 \text{ \AA}$ , or  $22 \text{ km s}^{-1}$  at the redshift of the Eagle (Gaussian  $\sigma = 8 \text{ km s}^{-1}$ ). The slit was oriented at the position angle of the photometric major axis which is  $49^\circ$  (east of north; upper left panel of Figure 2; measured in §4.5), which is approximately perpendicular to the gradient of the velocity field in Figure 1.

As in the IFS data, the spatially extended [OIII] emission line in the galaxy spectrum is used to measure gas rotation and dispersion profiles, but at 2D instead of 3D, and under the assumption of a spatially constant  $\sigma$ . The ROTCURVE fitting procedure of Weiner et al. (2006a) is used to fit a kinematic model. Briefly, this procedure fits Gaussians to each row of pixels in the emission line to obtain profiles of  $V$  and  $\sigma$  along the slit, and rejects discrepant values with automatic criteria (Figure 2, bottom panels). It then measures the light distribution along the slit and fits a Gaussian to it. Finally, ROTCURVE fits models of the position-velocity distribution along the slit, taking the seeing into account. The model has two parameters:  $V$  (not corrected for inclination) and  $\sigma$ . The resulting  $V$  and  $\sigma$  for the Eagle are  $0 \pm 9 \text{ km s}^{-1}$  and  $45 \pm 6 \text{ km s}^{-1}$ , respectively.

The 2D slit spectrum shows no evidence of rotation, whereas the 3D velocity field shows a rotation gradient of  $25 \pm 5 \text{ km s}^{-1}$ . This is because the slit was placed approximately perpendicular to the kinematic major axis. The  $\sigma$  measured from the slit spectrum is shown to be constant along the slit, as demonstrated by the Gaussian

fits to each row of the emission line (black points in the bottom left panel of Figure 2). The slit spectrum does not show the  $\sigma$  gradient found in the 3D  $\sigma$  map because it is luminosity-weighted and not as deep as the 3D observations. Therefore, it is biased towards the brightest regions of the galaxy (as depicted in the [OIII] line map in Figure 1), where the  $\sigma$  is  $55 \pm 10 \text{ km s}^{-1}$ .

This comparison between 2D and 3D spectroscopy of the same object demonstrates the power of 3D spectroscopy to reveal the full kinematics of high redshift galaxies.

#### 4.2 Star-formation rate

Historically, there are two main approaches to determine the star-formation rate (SFR) of a galaxy. These depend on the wavelength of the data at hand: optical or UV which trace the output of hot young stars (but which need to be corrected for interstellar extinction), and far-infrared which acts as a calorimeter (e.g., Kennicutt 1998). As multi-wavelength observations become more commonplace, studies of galaxy SFRs increasingly combine UV/optical and infrared indicators to obtain better accuracy (e.g., Dale et al. 2007; Calzetti et al. 2007; Kennicutt et al. 2009). These studies take advantage of the fact that dust mostly radiates in the infrared and sub-mm, while intercepting radiation at UV and optical wavelengths. Therefore, the addition of a UV or optically-determined SFR (not corrected for dust) and an infrared-determined SFR gives a more accurate account of the total SFR of a system. Furthermore, a comparison of the two SFRs gives insight into dust content.

Measurements of SFRs from far-infrared data rely on stellar models to predict the energy output from stars, and assume that most of the radiation from young stars is extinguished and re-processed into the infrared. A SFR is derived from the  $24\mu\text{m}$  flux of the Eagle following Noeske et al. (2007) using spectral energy distribution (SED) templates from Chary & Elbaz (2001). A Kroupa (2002) initial mass function is assumed, which does not differ significantly for the purposes of this paper from a Chabrier (2003) IMF (Rieke et al. 2009). The resulting SFR for  $F_{24\mu\text{m}} = 71.8 \pm 2.6 \mu\text{Jy}$  is  $6 \text{ M}_\odot \text{ yr}^{-1}$ , which has a factor of  $\sim 2$  uncertainty. This is consistent with SFRs derived with the formulations of Rieke et al. (2009) and Dale & Helou (2002).

SFRs derived from nebular emission lines (like  $H\beta$  which is used here) rely on stellar models to predict the ionizing luminosity of O stars. They assume that the extinction of the recombination photons is given by the Balmer decrement (i.e.,  $H\beta/H\alpha$ ). A calibration from Kennicutt (1998) for  $H\alpha$  line luminosity is typically adopted:  $\text{SFR (M}_\odot \text{ yr}^{-1}) = 7.9 \times 10^{-42} L(H\alpha) \text{ (ergs s}^{-1})$ . The resulting SFR is for a Salpeter (1955) IMF and is converted

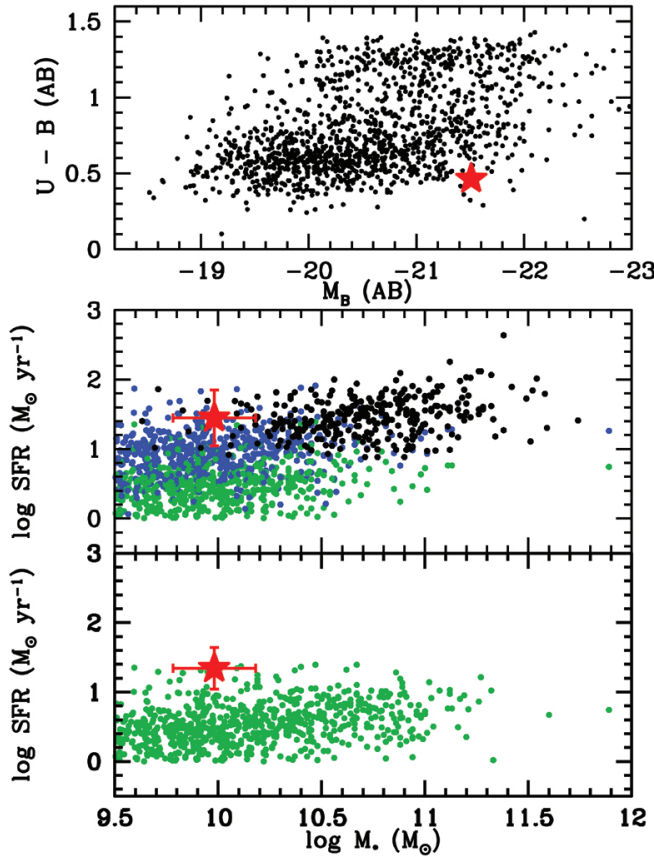


**Figure 4.** The Eagle galaxy (red star) is compared with galaxies at  $0.65 < z < 0.85$  in the AEGIS survey (points) in colour-magnitude and SFR- $M_*$  space. Top: A colour-magnitude diagram (not corrected for dust) shows that the Eagle is on the very bright and blue end of the distribution of galaxies at similar redshifts. Uncertainties on magnitudes are 10%. Middle: A SFR- $M_*$  diagram where the SFR is derived from line emission for blue galaxies with  $F_{24\mu m} < 60 \mu\text{Jy}$  with and without correcting for extinction (blue and green points, respectively), and from line emission and far-infrared flux for galaxies with  $F_{24\mu m} > 60 \mu\text{Jy}$  (black points). Uncertainties on SFRs and  $M_*$ 's are 0.2 dex. The Eagle has a high total SFR for its  $M_*$ . Bottom: This is the same as the middle plot except only the uncorrected SFRs derived from emission lines are plotted. The Eagle has a high SFR as derived from emission lines.

to a Chabrier (2003) IMF by a multiplicative factor of 0.66 (Rieke et al. 2009).

An  $H\beta$  line luminosity is adopted from the DEEP2 spectrum since the Eagle is compared with galaxies in DEEP2 for which measurements and calibrations are performed in the same manner. The  $H\beta$  line luminosity is measured following Weiner et al. (2007), and is  $10^{41.9 \pm 0.1} \text{ ergs s}^{-1}$ .

A *lower limit* to the emission line-determined SFR of the Eagle is derived from the  $H\beta$  line under the assumption of *no extinction* (i.e., case B recombination at  $10,000^\circ\text{K}$ :  $H\beta/H\alpha = 0.35$ , Osterbrock 1989), namely  $11.3 M_\odot \text{ yr}^{-1}$ . An *upper limit* is derived using a lower bound to the Balmer decrement for a distribution of blue galaxies in DEEP2 over  $0.33 < z < 0.39$  (the redshift range where both lines can be measured) from Weiner et al. (2007),

namely 0.11. This results in a SFR of  $36.0 M_\odot \text{ yr}^{-1}$ . Finally, to estimate the *mean* SFR of the Eagle from its  $H\beta$  line luminosity, the average Balmer decrement for galaxies in Weiner et al. (2007) is adopted, namely 0.198. This results in a SFR of  $20.3 M_\odot \text{ yr}^{-1}$ . In summary, the SFR of the Eagle derived from  $H\beta$  and not corrected further for extinction is  $20.3 M_\odot \text{ yr}^{-1}$  for a Chabrier (2003) IMF, with lower and upper limits of  $11.3$  and  $36.0 M_\odot \text{ yr}^{-1}$ , respectively. In this paper, we adopt the mean SFR since we know there is some dust present due to its detection at  $24\mu m$ .

SFRs derived from UV flux rely on stellar models to predict the UV flux from O and B stars and assume that the extinction is given by a measurement of the UV slope. Because intermediate-age stars also contribute to the UV flux, a simultaneous fit is typically made to the young and older stellar populations, and a dust model is assumed. Such a fit for the Eagle is adopted from Salim et al. (2009) and results in a SFR of  $9.4 \pm 2.0 M_\odot \text{ yr}^{-1}$  (corrected for extinction with the UV slope). The uncorrected value is  $3.5 M_\odot \text{ yr}^{-1}$ . The discrepancy between this measurement and the  $H\beta$ -derived SFR is somewhat unusual. Along with the low  $24\mu m$ -derived SFR, it is evidence that extinction is low in star-forming regions in the Eagle.

The SFR from the  $24\mu m$  flux ( $6 M_\odot \text{ yr}^{-1}$ ) is less than even the lower limit to the SFR derived from  $H\beta$  which is not corrected for extinction ( $11.3 M_\odot \text{ yr}^{-1}$ ). Even though both these measurements are uncertain to within a factor of  $\sim 2$  due to statistical scatter in the flux-to-SFR conversion, they differ systematically. The SFR derived from  $24\mu m$  is calculated under the assumption that dust captures all the UV flux (calorimeter assumption), and the SFR derived from  $H\beta$  with zero dust correction ( $11.3 M_\odot \text{ yr}^{-1}$ , lower limit) assumed that dust captures none of the ionizing or  $H\beta$  flux. For the vast majority of galaxies in the DEEP2 Survey, the SFR derived from  $24\mu m$  is greater than the uncorrected line-derived SFR by a factor of  $\sim 3$ . There are hardly any galaxies where the uncorrected emission line-derived SFR is greater than the  $24\mu m$ -derived SFR. The Eagle is an exception as its emission-line SFR is greater by at least a factor of  $\sim 2$  ( $11.3$  versus  $6 M_\odot \text{ yr}^{-1}$ ). Similarly, Bell et al. (2005) find the  $24\mu m$ -derived SFR dominates the uncorrected UV-derived SFR.

This discrepancy between  $24\mu m$  and uncorrected  $H\beta$ -derived SFRs suggests that the fraction of line emission escaping the sites of star-formation is large so that the calorimeter assumption is violated and the extinction of  $H\alpha$  could be lower than normal. In addition, a low dust content is consistent with the blue colour of the galaxy, uncorrected for dust (Figure 4, top panel). A total SFR for the Eagle is estimated by adding the emission line (not corrected for dust) and  $24\mu m$ -derived SFRs, and results in  $26.3 M_\odot \text{ yr}^{-1}$ , which has a factor of 2–3 uncertainty.

To compare the Eagle with galaxies at similar redshifts, in Figure 4 the SFRs of galaxies in the AEGIS Survey at  $0.65 < z < 0.85$  are plotted versus stellar mass (following Noeske et al. 2007), and the Eagle galaxy is highlighted. The sample is  $> 80\%$  complete for  $M_* \gtrsim 10^{9.6} M_\odot$  and  $> 95\%$  complete for  $M_* \gtrsim 10^{10}$  (Noeske et al. 2007). These galaxies are from the same data set and

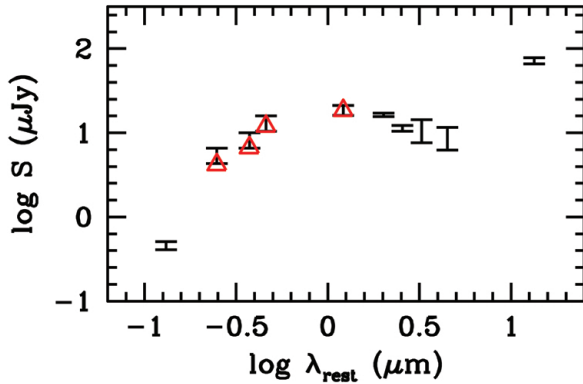


**Figure 5.** Multi-wavelength broad band spectral energy distribution of the Eagle galaxy (black error bars) and the best-fit galaxy stellar population model to the optical and near-infrared fluxes from Bundy et al. 2006 (red triangles). The data, from left to right, are *NUV*, *B*, *R*, *I*, *K*, IRAC channels 1, 2, 3, 4, and MIPS 24 $\mu$ m fluxes. The fluxes are  $\log S = -0.34 \pm 0.05, 0.726 \pm 0.09, 0.908 \pm 0.09, 1.111 \pm 0.09, 1.213 \pm 0.02, 1.053 \pm 0.03, 1.018 \pm 0.14, 0.930 \pm 0.14, \text{ and } 1.856 \pm 0.04 \mu\text{Jy}$ , respectively.

have SFRs measured in a homogeneous manner. Figure 4 shows that the Eagle has a high SFR compared to galaxies at similar stellar masses, even when only the SFR derived from line emission is taken into account.

#### 4.3 Stellar mass & broad-band spectral energy distribution

The multi-wavelength SED for the Eagle galaxy is shown in Figure 5. Fits of galaxy stellar population models to the observed *B*, *R*, *I*, and *K<sub>s</sub>*-band fluxes were performed by Bundy et al. (2006) to obtain a stellar mass estimate ( $M_*$ ) for the Eagle. These are the wavelengths at which stellar population models are the best-characterised. The galaxy models constituted a grid of synthetic spectral energy distributions from Bruzual & Charlot (2003) which spanned a range of exponential star-formation histories, ages (restricted to be less than the age of the Universe at the redshift of the Eagle), metallicities, and dust contents. A Chabrier (2003) initial mass function, which does not differ significantly from the Kroupa (2002) function assumed for the SFR calculation, was adopted. At each point on the grid of models, the following is calculated: the *K<sub>s</sub>*-band stellar mass-to-light ratio, minimum  $\chi^2$ , and probability that each model accurately describes the galaxy. The corresponding  $M_*$  is then determined by scaling the stellar mass-to-light ratio to the *K<sub>s</sub>*-band luminosity based on the total *K<sub>s</sub>*-band magnitude. The probabilities are then summed (marginalised) across the grid and binned by model stellar mass, yielding a stellar mass probability distribution for the galaxy. The median of the distribution is adopted as the best estimate. The  $M_*$  measured in this way is robust to degeneracies in the models, such as those between age and metallicity (Bundy et al. 2006). The best-fit model has a  $\log M_*$  of  $10.0 \pm 0.2 M_\odot$ , where the uncertainty is taken from the width of the probability distribution. There are additional systematic uncertainties associated with the IMF

and stellar population synthesis models adopted which can be as large as 0.4 dex (Barro et al. 2011). At the redshift of the Eagle, taking into account the TP-AGB phase of stellar evolution does not produce significant changes in stellar mass estimates (e.g., Barro et al. 2011).

We refrain from including the IRAC channel 1 waveband in the SED fit since doing so decreases the goodness of the model fit. This is possibly because of uncertainties in stellar population models at this wavelength. The mid to far-infrared points are not included in the fit because stellar population models do not currently include the dust modelling necessary to fit them. Furthermore, although the best-fit model also provides estimates of age, metallicity, star-formation history, and dust content, these quantities are much more affected by degeneracies and are poorly constrained compared with the stellar mass (Bundy et al. 2006).

#### 4.4 Test for AGN contamination

In this section, we test for active galactic nuclei, or AGN, contribution to the emission lines in the spectrum of the Eagle. This could affect derived quantities such as kinematics, SFR, and stellar mass. There are two methods which are regarded as the most effective for the detection of AGN in high redshift galaxies, where it is generally not possible to isolate the nuclear regions. These are optical emission line and X-ray selections. Neither selection is perfect. Emission lines from the AGN can be overpowered by star-formation, and X-rays can be affected by heavy absorption of gas in close proximity to the AGN. However, a combination of these two methods is the best currently available to identify AGN (Yan et al. 2010).

To test for a possible contribution from AGN to the Eagle, we first look to an emission line diagnostic diagram derived for galaxies in the DEEP2 Survey over  $0.3 < z < 0.8$  (Yan et al. 2010, Figure 5). This diagram uses integrated rest-frame  $U - B$  colour and  $[\text{OIII}]/\text{H}\beta$  line ratio to separate star-forming galaxies from AGN. The Eagle galaxy lies in the star-forming region of the diagram given its  $[\text{OIII}]/\text{H}\beta$  value of  $0.53 \pm 0.2$  from the DEEP2 spectrum.

Next, we look to the deep 200ks Chandra data. No counts were detected at the coordinates of the Eagle in either of the Chandra bands. This places  $5\sigma$  upper limits on the X-ray luminosity of AGN in the Eagle of  $L_X = 1.1 \times 10^{-16}$  and  $8.2 \times 10^{-16}$  ergs  $\text{s}^{-1} \text{ cm}^{-2}$  for the soft and hard bands, respectively.

Furthermore, we note that the near-infrared through IRAC portion of the SED in Figure 5 does not show the typical power law shape of an AGN. In conclusion, the kinematics and emission line luminosities of the Eagle are likely not strongly affected by AGN.

#### 4.5 Metallicity

The oxygen abundances of the Eagle and galaxies in AEGIS at similar redshifts ( $0.65 < z < 0.85$ ) are estimated. This is done by adopting the relation between  $R_{23}$  and the gas phase oxygen abundance by McGaugh

(2001), following Kobulnicky & Kewley (2004). The upper branch of this calibration is adopted because the majority of galaxies in Kobulnicky & Kewley (2004) and Kobulnicky & Zaritsky (1999) with NII/H $\alpha$  measurements fall there. This measurement relies on equivalent widths of emission lines. It works in part because star-forming galaxies have a relatively narrow range of continuum shapes between [OII] and [OIII], and do not have large 4000Å breaks. For the Eagle, rest-frame equivalent widths of the [OII]  $\lambda 3727$ , [OIII]  $\lambda 5007$ , and H $\beta$  lines ( $67.00 \pm 1.25$ ,  $77.33 \pm 1.82$ , and  $28.1 \pm 0.73$ , respectively and all in Å), result in an oxygen abundance of  $12 + \log(\text{O}/\text{H}) = 8.66 \pm 0.05$ .

In Figure 6, the oxygen abundances of AEGIS galaxies and the Eagle are plotted versus rest-frame  $B$ -band magnitudes and Petrosian radii (measured from  $I$ -band *Hubble* images as described below). This galaxy sample is complete down to at least  $M_B$  (AB)  $\lesssim 19$  for blue galaxies (no red galaxies are shown in the figure) in the redshift range plotted (Willmer et al. 2006). Galaxies from Kobulnicky & Kewley (2004) in the same redshift range are also compared. The Eagle galaxy is brighter by  $\sim 2$   $B$ -band magnitudes and larger by  $\sim 0.4$  dex than average for its oxygen abundance. The oxygen abundance of the Eagle is similar to those of galaxies at similar stellar masses in the IMAGES Survey at  $z \sim 0.6$  (Rodrigues et al. 2008).

## 5 A DISTURBED AND HIGHLY STAR-FORMING GALAXY

The SWIFT 3D kinematic fields demonstrate that the Eagle galaxy has a gradient in  $\sigma$  which ranges from  $35 - 75 \pm 10 \text{ km s}^{-1}$  and a  $V$  of at least  $25 \pm 5 \text{ km s}^{-1}$ . Whatever the process (or processes) is that creates the abnormally high  $\sigma$  values, it is likely active throughout most of the galaxy. These  $\sigma$  values are likely caused by the blurring of velocity gradients, which may not even have a preferred plane, on scales at or below the seeing limit (Weiner et al. 2006a; Kassin et al. 2007). The high  $\sigma$ 's are consistent with the morphology of the Eagle, which is quantitatively classified as a major merger, and shows structures unlike those of a normal disc galaxy.

Table 1 summarises the properties of the Eagle galaxy, and Figures 3–6 compare it with galaxies at the same epoch. Compared to these galaxies, the Eagle is extremely bright and blue in the rest-frame optical. It is highly star-forming with an unusually high SFR as derived from line emission, and a comparably low SFR as derived from far-infrared luminosity. This suggests that most of the star-formation in the Eagle occurs in dust-free regions. The Eagle is also large and bright for its metallicity. These properties are not surprising given that the Eagle was primarily selected to have extended and bright emission lines.

The Eagle could be in an early stage of a star-burst brought on by a major merger. It may have not yet had enough time for metal enrichment, or to have formed the mass of dust typically found in highly star-forming galaxies. It is possible that the high SFR could drive winds that expose star-forming regions, and, given the lower metallicity, may explain the low extinction. (There are local

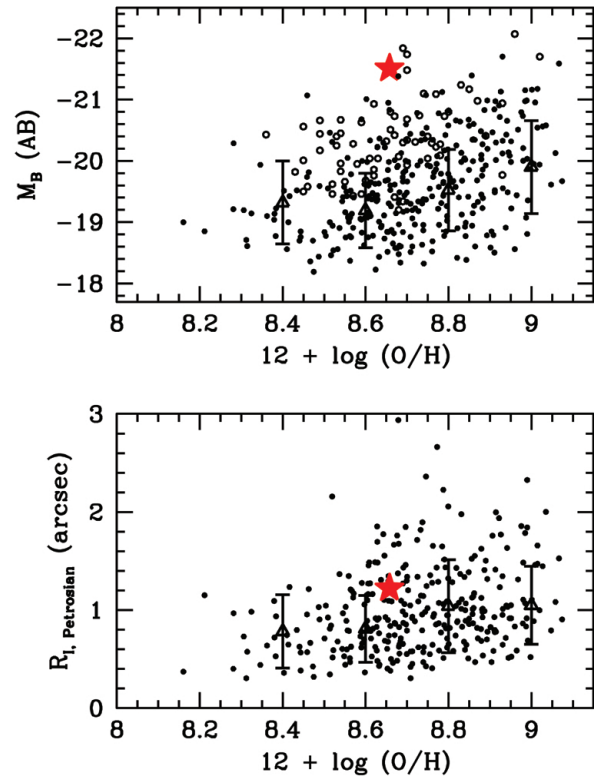


**Figure 6.** Oxygen abundances are compared with rest-frame  $B$ -band magnitudes (top) and  $I$ -band Petrosian radii (bottom) for galaxies in the AEGIS Survey at  $0.65 < z < 0.85$  (filled circles) and from Kobulnicky & Kewley (2004) (open circles). Typical uncertainties in the measurements of oxygen abundances, sizes, and  $B$ -band magnitudes are 0.05 dex, 0.1 dex, and 10%, respectively. In addition, for the oxygen abundances, there can be systematic errors in the calibration which may be  $> 0.1$  dex (Kobulnicky & Kewley 2004). Binned averages for the AEGIS galaxies are shown as open triangles and error bars show the rms scatter. The Eagle galaxy is plotted as a red star. It is bright and large for its oxygen abundance.

dwarf galaxies which show similar phenomena, but this galaxy is much more massive than such systems.) The low metallicity and strong star-burst may also be explained by a major merger event that brings lower metallicity gas from the outer parts to the centre of the system (e.g., Kewley, Geller, & Barton 2006).

It is likely that the mechanism which causes the star burst is the same, or initiated by, that which causes the high velocity dispersion and disturbed morphology. This mechanism is likely a major merger.

## ACKNOWLEDGMENTS

The Oxford SWIFT integral field spectrograph is directly supported by a Marie Curie Excellence Grant from the European Commission (MEXT-CT-2003-002792, Team Leader: N. Thatte). It is also supported by additional funds from the University of Oxford Physics Department and the John Fell OUP Research Fund. Additional funds to host and support SWIFT were provided by Caltech Optical Observatories.

This paper is based in part on observations obtained at the Hale Telescope at Palomar Observatory as part of a collaborative agreement between the California Institute of Technology, its divisions Caltech Optical Observatories and the Jet Propulsion Laboratory (operated for NASA), and Cornell University.

Additional support was provided for by the Observational Astrophysics Rolling Grant at Oxford and the Oxford Astrophysics PATT Linked Grant ST/G004331/1. The following NSF grants to the DEEP2 Survey are acknowledged: AST00-71198, AST05-07483, and AST08-08133.

L. Fogarty would like to acknowledge the generous support of the Foley-Béjar Scholarship through Balliol College, Oxford and the support of the STFC.

This work of LAM was carried out in part at Jet Propulsion Laboratory, California Institute of Technology, under a contract with NASA. LAM acknowledges support from the NASA ATFP program.

## REFERENCES

- Abraham, R. G. et al. 1996, *ApJS*, 107, 1  
 Abuter, R. et al. 2006, *New Astron. Reviews*, 50, 398  
 Baldwin, J. A., Phillips, M. M., & Terlevich, R. 1981, *PASP*, 93, 5  
 Barro, G. et al. 2011, *ApJS*, 193, 30  
 Bell, E. F. et al. 2004, *ApJ*, 608, 752  
 Bell, E. F. et al. 2005, *ApJ*, 625, 23  
 Bershad, M. A. et al. 2000, *AJ*, 119, 2645  
 Bertin, E. & Arnouts, B. 1996, *A&AS*, 117, 393  
 Bruzual, G. & Charlot, S. 2003, *MNRAS*, 344, 1000  
 Bundy, K. et al. 2006, *ApJ*, 651, 120  
 Calzetti, D. et al. 2007, *ApJ*, 666, 870  
 Chabrier, G. 2003, *PASP*, 115, 763  
 Chary, R. & Elbaz, D. 2001, *ApJ*, 556, 562  
 Choi, P. et al. 2006, *ApJ*, 637, 227  
 Coil, A. L. et al. 2004, *ApJ*, 617, 765  
 Conselice, C. J. et al. 2003, *AJ*, 126, 1183  
 Covington, M. D. et al. 2010, *ApJ*, 710, 279  
 Cresci, G. et al. 2009, 697, 115  
 Davis, M., et al. 2003, *Proc. SPIE*, 4834, 161  
 Davis, M., et al. 2007, *ApJ*, 660, L1  
 Dale, D. A. & Helou, G. 2002, *ApJ*, 576, 159  
 Dale, D. A. et al. 2007, *ApJ*, 655, 863  
 Epinat, B. et al. 2009, *A&A*, 504, 789  
 Epinat, B. et al. 2010, *MNRAS*, 401, 2113  
 Faber, S. M. et al. 2007, *ApJ*, 665, 265  
 Flores, H. et al. 2006, *A&A*, 455, 107  
 Fogarty, L. et al., *MNRAS*, submitted  
 Förster Schreiber, N. et al. 2006, *ApJ*, 645, 1062  
 Förster Schreiber, N. et al. 2009, *ApJ*, 706, 1364  
 Fuentes-Carrera, I. et al. 2010, *A&A*, 513, 43  
 Hammer, F. et al. 2009, *A&A*, 496, 381  
 Kassin, S. A. et al. 2007, *ApJ*, 660, L35  
 Kennicutt, R. C. 1998, *ApJ*, 498, 541  
 Kennicutt, R. C. et al. 2009, *ApJ*, 703, 1672  
 Kobulnicky, H. A. & Zaritsky, D. 1999, *ApJ*, 511, 118  
 Kobulnicky, H. A. & Kewley, L. J. 2004, *ApJ*, 617, 240  
 Kewley, L. J., Geller, M. J., & Barton, E. J. 2006, *AJ*, 131, 2004  
 Kroupa, P. 2002, *Science*, 295, 82  
 Law, D. R. et al. 2009, *ApJ*, 697, 2057  
 Lemoine-Busserolle, M. & Lamareille, F. 2010, *MNRAS*, 402, 2291  
 Lemoine-Busserolle, M. et al. 2010 *MNRAS*, 401, 1657  
 Lin, L. et al. 2007, *ApJ*, 660, L51  
 Lotz, J. M., Primack, J., & Madau, P. 2004, *AJ*, 128, 163  
 Lotz, J. M. et al. 2008, *ApJ*, 672, 177  
 McGaugh, S. S. 1991, *ApJ*, 380, 140  
 Massey et al. 2004, *MNRAS*, 348, 214  
 Neichel, B. et al. 2008, *A&A*, 484, 159  
 Noeske, K. G. et al. 2007, *ApJ*, 660, L43  
 Oesch, P. A. et al. 2010, *ApJ*, 714, L47  
 Osterbrock, D. E. 1989, *Astrophysics of gaseous nebulae and active galactic nuclei* (University Science Books)  
 Peirani, S. et al. 2009, *A&A*, 496, 51  
 Petrosian, V. 1976, *ApJ*, 209, L1  
 Puech, M. et al. 2007, *A&A*, 466, 83  
 Puech, M. et al. 2008, *A&A*, 484, 173  
 Puech, M. et al. 2009, *A&A*, 493, 899  
 Puech, M. et al. 2010, *MNRAS*, 406, 535  
 Puech, M. et al. 2010, *A&A*, 510, A68  
 Rieke, G. H., Loken, K., Rieke, M. J., & Tamblyn, P. 1993, *ApJ*, 412, 99  
 Rieke, G. H. et al. 2009, *ApJ*, 692, 556  
 Rodrigues, M. et al. 2008, *A&A*, 492, 371  
 Salim, S. et al. 2009, *ApJ*, 700, 161  
 Salpeter, E. E. 1955, *ApJ*, 121, 161  
 Schreiber, J. et al. 2004, in *ASP Conf. Ser.* 314, *Astronomical Data Analysis Software and Systems (ADASS) XIII*, ed. F. Ochsenbein, M. G. Allen, & D. Egret (San Francisco: ASP), 380  
 Strateva, I. et al. 2001, *AJ*, 122, 1861  
 Thatte, N. et al. 2006, *Proc. SPIE*, 6269, 113  
 van Dokkum, P. G. 2001, *PASP*, 113, 1420  
 van Starkenburg, L. et al. 2008, *A&A*, 488, 99  
 Weiner, B. J. et al. 2006a, *ApJ*, 653, 1027  
 Weiner, B. J. et al. 2006b, *ApJ*, 653, 1049  
 Weiner, B. J. et al. 2007, *ApJ*, 660, L39  
 White, S. D. M. & Frenk, C. S. 1991, *ApJ*, 379, 52  
 Willmer, C. N. A. et al. 2006, *ApJ*, 647, 853  
 Wirth, G. D. et al. 2004, *AJ*, 127, 3121  
 White S. D. M., 1996, in Schaefer R., Silk J., Spiro M., Zinn-Justin J., eds, *Cosmology and Large-Scale Structure*. Elsevier, Dordrecht, astro-ph/9410043  
 Wright, S. et al. 2009, *ApJ*, 699, 421  
 Yan, R. et al. 2011, *ApJ*, 728, 38  
 Yang, Y. et al. 2008, *A&A*, 477, 789